Machine Learning techniques for solar irradiation nowcasting: Cloud type classification forecast through satellite data and imagery

Alfredo Nespoli [a,1], Alessandro Niccolai [a,1,*], Emanuele Ogliari [a,1], Giovanni Perego [b,1], Elena Collino [c,1], Dario Ronzio [c,1]

[a] *Politecnico di Milano, Dipartimento di Energia, Via La Masa, 34, 20156 Milan, Italy*
[b] *Bluefondation, Monticello, 23876 Brianza, Italy*
[c] *RSE S.p.A. - Ricerca sul Sistema Energetico, via R. Rubattino 54, 20134 Milano, Italy*

A B S T R A C T

One of the most important modern challenges in making the renewable energy sources more reliable is the development of new tools to better manage their non programmable nature and avoid economic losses, to ensure compliance with network constraints and to improve the management of congestion. The solar energy at ground level exhibits a continuous variation in time and space. This fluctuation has a deterministic component generated by the movements of rotation and revolution of the earth, and a random one generated by weather conditions. Solar energy variations at ground level have a great influence on the output power of a photovoltaic plant, which can fluctuate significantly in short intervals due to the random component. This work presents a new model to detect in real time the clouds which potentially obstruct the sunrays directed to a specific geographic target. Moreover, a novel procedure for the forecasting of the clearness sky index on the target in the fifteen minutes is proposed, levereging on Machine Learning techniques, exploiting satellite and weather data.

1. Introduction

The growth of the variable Renewable Energy Sources (RES), boosted by the environmental challenges [1], is posing new issues in the management of electrical grid. Electrical Energy Storage Systems can provide a viable solution for residential applications [2], while for larger scale plants most of the effort are devoted to the definition of accurate production forecasting techniques [3,4].

Very attractive from environmental and economic perspectives, renewable energy sources (RES) can provide significant challenges since energy production depends on external weather factors that cannot be controlled [5,6].

The power generated by a photovoltaic (PV) module depends on cloud cover, sun position, weather conditions, etc. all of which can dramatically vary throughout the course of a single day [7]. To fully integrate and efficiently manage the solar power into the existing grids, the future power output must be known [8,9]. Regarding systems such as microgrids, the RES fluctuation can be compensated by backup technologies and energy storage, which should be properly sized and coordinated, with the purpose of increasing the efficiency, reduce the

fuel consumption or a wise combination the two [10,11]. An accurate PV power forecast can greatly help operations, unit commitment and, on a longer time horizon, sizing of available units, ultimately reducing the investment costs [12].

From the Energy Management System (EMS) perspective, a 24-hours ahead forecast is needed to perform an initial optimization of the system management, with the goal of, for example, minimizing the operating cost, reducing the fuel consumption over the following 24 h [13,14]. Approaching the operating time, additional refinements are useful to further correct the original forecast and tune the dispatching schedule in the so-called intraday forecast [15]. Eventually, during the operations, an integration of the previous forecast for the following minutes is required for the predictive power management [16].

For this reason, the problem of forecasting the future energy produced from PV modules has been extensively studied in the literature. Indeed, a wide variety of solutions from short- to long-term forecasting have been proposed [17,18].

According to Antonanzas et al. [19], the classification of these models, based on the forecasting temporal horizon leads to define

four main groups: two days ahead or longer, six hours to day ahead, intra-day, and intra-hour or nowcasting.

The work presented here is focused the on very short-term forecasting, which generally covers horizons from few seconds to 30 min. This particular type of foresting is crucial for the grid management because it allows to ensure grid stability, power quality, and to correctly schedule spinning reserves and demand response. The main issue is related to the identification of the sudden spikes and drops in the PV power production. These fluctuations are mainly related to the presence of moving clouds, which hinder solar radiation [20]. For this reason, most of the work found in literature relies on the adoption of satellite images and whole sky images [21,22].

As regards the methodologies developed so far to carry out the PV power forecasting, models are divided by [19] into two groups based on the techniques adopted, i.e. physical, and statistical models. The first option consists in using analytical equations to model the PV system. Physical methods are mainly used for their deterministic approach, allowing them to be the winning choice to quickly get the results employing a mathematical model [23]. The literature also proposes specific PV cell models to predict solar energy production. An example is the one by Dolara et al. [24] that consists in the combination of cell equivalent circuit, with the irradiance model, and PV cell thermal models to predict the PV power production. This methodology requires three different types of input: date and time, meteorological conditions, and the characteristic of the PV panel.

Statistical models are characterized by the use of historical data to learn the characteristics of a process and make forecasts of complex problems on the basis of the knowledge acquired during a training period. These historical information is usually a voluminous amounts of structured or unstructured data that becomes complex to be processed by traditional data processing techniques and platforms, but can be easily analyzed by statistical models [25]. Antonanzas et al. [19], classify the statistical models into two main categories: Regressive methods and Artificial Intelligence (AI) techniques. The Regressive methods estimate the relationship between a dependent variable (solar power output) and some independent variables, called predictors.

The most commonly used Artificial Intelligence techniques are Artificial Neural Networks (ANN) and Random Forest (RF).

A neural network is a general mathematical computing paradigm that models the operations of biological neural systems. Although ANNs, while implemented on computers are not programmed to perform specific tasks, they are trained with datasets to learn patterns and make previsions [26], and they are widely used for PV forecasting. In their work, Mellit et al. [27], present a particular method for solar irradiance forecast using Artificial Neural Network that exploits the mean daily solar irradiance and air temperature. In another study, T. A. Siddiqui et al. [28], propose the application of a deep neural network approach to observe and estimate short-term weather effects from time-lapsed videos (sky-videos), in order to make forecasts of surface irradiance.

Random Forest is the most trusted classifier technique by data experts. It consists of an ensemble of decision trees that represent a distinct instance of the classification of the input data [29,30]. Although RF are rarely used for PV forecasting, they show very positive results whenever they are applied. For example, the work proposed by Tato et al. [31] aims at combining simple radiation predictions with real radiation measurements to forecast the solar photovoltaic energy production of a diverse variety of PV modules for short-term temporal horizons. Moreover, the work presented by Meng et al. [32] uses the Random Forests to predict the daily PV power generation by means of weather measures.

All the forecasting approaches presented above can also be integrated with optimization methods, obtaining an effective Decision Support System for grid management [33].

To improve the performance of the physical and statistical models, they can be combined with the goal to join the strengths of each model in a single one able to better achieve the goal [15]. The review proposed by Akhter et al. [34] shows how the hybrid techniques produce better forecasting accuracy for solar power output, in comparison to individual machine learning (ANN, SVM, ELM) and mathematical techniques. One example is the work made by Dolara et al. [35], in which is designed a new auxiliary hybrid system model called Physical Hybridized Artificial Neural Network (PHANN), which combines an artificial intelligence technique (ANN) with an analytical physical model: The Clear Sky Solar Radiation Model (CSRM).

The power produced by a photovoltaic plant mainly depends on two factors: the sun position in the sky (i.e. the incidence angle of the direct rays) and the attenuation of the radiation from the Earth's atmosphere [36]. While the first factor is easily predictable through the application of precise mathematical models, the main cause of the reduction of solar radiation to the ground is attributable to the presence of cloud cover [37]. The forecast of cloud cover is therefore an essential factor for determining the irradiation on the ground and the production of a photovoltaic system [38,39]. This problem can be approached through satellite images which are exploited by Machine Learning (ML) techniques, for the determination and forecasting of the solar irradiance at ground level [40–42].

The work presented by H.S. Jang et al. [43] exploits these techniques by proposing a solar power prediction model based on various satellite images and a Support Vector Machine (SVM) learning scheme. Furthermore N.A. Engerer et al. [44] designed a methodology to produce real-time PV power estimates as derived from Himawari-8 satellite imagery, and validating them against seven Australian radiation monitoring sites and 78 small-scale Behind-the-Meter solar PV sites.

In light of the above, the attenuation of the solar radiation from the atmosphere depends on various factors and it cannot be precisely modeled by physical laws because of its aleatory nature. However, in order to forecast the power produced by a PV plant in the short term, it is essential to predict this attenuation. The attenuation is well described by means of the Clearness index which is defined as the ratio of global solar irradiance measured at ground level and the global solar irradiance that would be measured at same time but with clear sky conditions.

The purpose of this work is to forecast the fifteen minutes ahead solar irradiance, hitting a precise target, by means of Machine Learning techniques, satellite images and weather data. Several novelties were introduced in the present work. Firstly, a new model which is able to detect in real time the clouds which potentially interfere with the sunbeams directed to a target point is designed. The aim of this model is to allow a reduction of the training effort of machine learning techniques without a reduction of the forecasting accuracy. With respect to the state of the art, the novelty is the implementation of a light and effective method for the short term forecast of peaks and drops in the solar radiation in a given location. Secondly, based on the previous step, three different Machine Learning models for the solar irradiance forecasting at ground level have been developed and tested. The proposed models have been tested in Milan, at the Solar Tech Lab. The Solar Tech Lab (latitude 45.502921°N; longitude 9.156564°E), located on the roof of the Energy department building of the Politecnico di Milano, hosts a facility for PV panels test and a meteorological station.

This paper is structured as follows. Section 2 describes the design and implementation process of the Cloud model and presents the obtained results. The three different Machine Learning techniques used are described in detail in Section 3. In Section 4, the case study is presented, while, in Section 5, the results of the irradiance forecasts are reported. Lastly, some conclusions are drawn in Section 6.

2. Cloud model

The objective of this model is to identify the presence of clouds that can potentially interact with the sunrays directed to a precise target, exploiting meteorological satellite data.

For the purpose of this work, the geographic reference point is the Solar Tech Lab (latitude 45.502921° N; longitude 9.156564° E), located on the roof of the Energy department building of the Politecnico di Milano.

2.1. Satellite data

In order to evaluate the attenuation of the income solar radiation on the target, the information on the cloudiness has been derived from Meteosat Second Generation (MSG) satellite data. The Spinning Enhanced Visible and InfraRed Imager (SEVIRI) on board the geostationary MSG, provides irradiation data in twelve different spectral bands, every fifteen minutes on a large portion of the Earth, with a spatial resolution around 4.5 km on the Italian territory [45].

By means of the software SAFGEO [46], issued by EUMETSAT, the European Organization for the Exploitation of Meteorological Satellites, it is possible to classify each satellite pixel into 19 categories of clouds, by processing SEVIRI images in the twelve channels. The 19 types of cloud types are:

1. cloud free land;
2. cloud free sea;
3. land contaminated by snow;
4. sea contaminated by snow/ice;
5. very low and cumuliform clouds;
6. very low and stratiform clouds;
7. low and cumuliform clouds;
8. low and stratiform clouds;
9. medium and cumuliform clouds;
10. medium and stratiform clouds;
11. high opaque and cumuliform clouds;
12. high opaque and stratiform clouds;
13. very high opaque and cumuliform clouds;
14. very high opaque and stratiform clouds;
15. high semitransparent thin clouds;
16. high semitransparent meanly thick clouds;
17. high semitransparent thick clouds;
18. high semitransparent above low or medium clouds;
19. fractional clouds (sub-pixel water clouds).

An example of cloud classification, obtained from MSG, on the area surrounding the Solar Tech Lab is reported in Fig. 1.

2.2. Cloud model implementation

In order to determine which portion of the atmosphere is crossed by the sun's rays, the cloud cover and the path followed by the sunrays directed to the Solar Tech Lab are reconstructed.

First, the satellite image is divided in parallelograms and subsequently in each region the sky conditions reported by the correspondent pixel are shaped. As regards the extension of the area to be taken into account in order to consider all the possible interactions among sun rays and clouds affecting the target, it is important to consider that it varies according to the sun elevation. In particular, the portion of atmosphere to be considered at the instants following sunrise and preceding sunset is very big, therefore a compromise is sought between computational burden (image dimensions) and amount of time neglected in each day of analysis. The threshold of 10° of solar elevation has been chosen, corresponding to an extension of 18 × 51 pixels respectively in a north–south and east–west direction (Fig. 2). The decision arises out of the fact the amount of energy produced by PV modules is negligible under this sun elevation.

Then, the cloud top and bottom heights are taken into considerations to build the clouds. The first one can be estimated by crossing the cloud top temperature, obtained from satellite data with a vertical profile of the atmosphere, while the cloud bottom heights cannot be
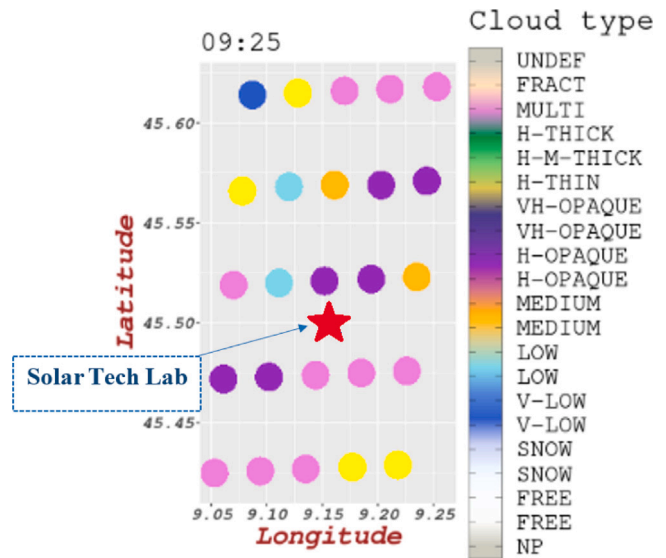

Fig. 1. Example of cloud type classification of the satellite pixels surrounding the Solar Tech Lab.

detected only by satellite data and it is therefore approximated with the minimum height at which each cloud type can be found in the troposphere. Last, the path followed by the sun's rays headed to the Solar Tech Lab is determined from the solar elevation and azimuth angles (α and γ respectively), computed by the PVLib Matlab function *pvl_ephemeris* [47], which takes as input date and time, latitude and longitude of the observation point.

This information allows to approximate the line joining the geographic target, with the apparent position of the sun. An example is depicted in Fig. 3, where the line is colored in red. In the same picture all the clouds are represented by means of parallelepipeds colored according to the corresponding cloud type.

After this setup, the model is able to determine if the clouds are present in the scene and could potentially interact with the sun rays by evaluating whether the red straight line depicted in Fig. 3 crosses one or more cloud boxes. The clouds giving interference are highlighted in red in the same figure.

If multiple cloud boxes are intercepted, two selection criteria are established in order to determine which pixel, among those selected, gives the greatest effect on the radiation. The first one evaluates the cloud classes and selects those that can more easily obstruct the direct rays, considering the characteristics related to the opacity of the clouds. If more than one cloud boxes are highlighted after this first selection, then the closest one to the Solar Tech Lab is chosen.

When no pixels are highlighted by the model it means that the direct rays do not encounter obstacles, and consequently the conditions representative of that satellite image are clear sky.

Fig. 4 reports a representation of the complete cloud model.

2.3. Correlation with GHI and cloud type clustering

The new Cloud model here presented allows to identify the portion of the sky that mostly interact with the direct sun rays and to identify the clouds that interact with the sunbeams. Secondly, this model is used to merge different types of clouds that show similar interacting behavior with the direct sunlight. Due to the large number of the classes provided by the SAFGEO software, an aggregation through a classification reduction can facilitate the work of the Machine Learning algorithms and finally better predict the solar irradiance as explained in the following.
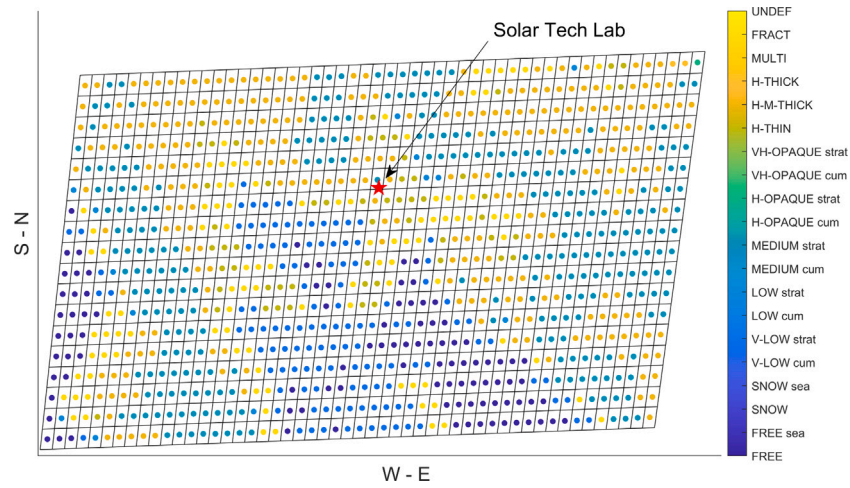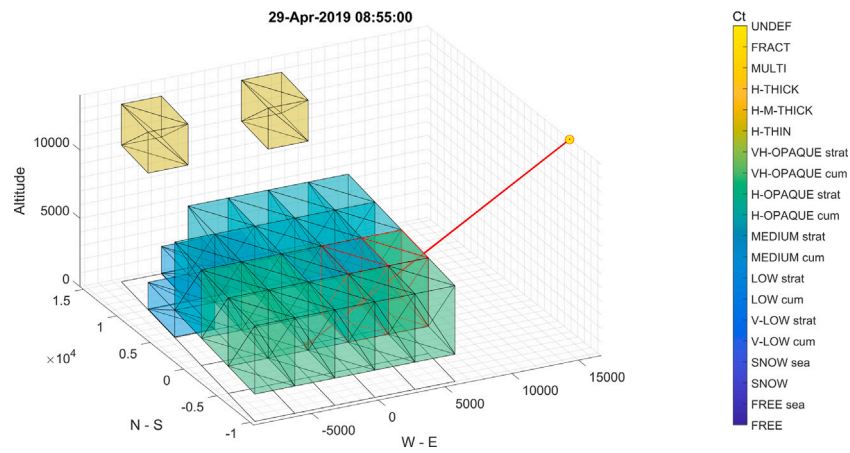
Fig. 2. Example of satellite picture 18 × 51.

Fig. 3. Example of a small sky portion of the cloud model with intercepted clouds.
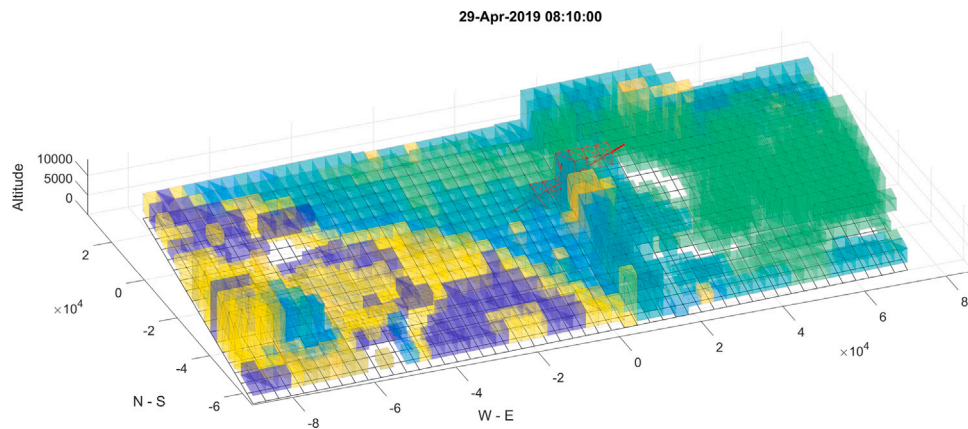

Fig. 4. Complete model (18 × 51 pixel).

For this reason, the objective is to find a correlation between the radiation measured at the Solar Tech Lab and the corresponding result obtained from the model described above. This allows to verify if it is possible to simplify the classification of the clouds, and therefore facilitate the prediction of solar radiation, which is explained in a following section.

The radiation reaching the ground depends on both the atmospheric conditions and the apparent position of the sun in the sky, i.e. the solar altitude angle. To decouple the measure of solar radiation from the position of the sun, it is computed the Clearness Index (Eq. (1)), which is the ratio between the GHI_m measured by a pyranometer placed at Solar Tech Lab, and the GHI_{cs} obtained by an Ineichen and Perez Clear Sky Model (CSM) [48].

$$K_T = \frac{GHI_m}{GHI_{cs}} \tag{1}$$

Satellite images are shot every fifteen minutes, while the irradiance measures are sampled every ten seconds. To overcome this asynchronism the average GHI is calculated averaging the measurements between 7 min before and 8 after the picture is taken. In the same way, the corresponding output values of the CSM are averaged.

It is now possible to investigate the presence of a correlation between the Clearness Index and the correspondent Ct contained in the pixel identified by the Cloud model already designed. The analysis shows a fair correlation between the Clearness Index and the class of the cloud that intercepts the sun's rays. Considering the use of Machine Learning algorithms for making solar irradiation forecasting, it is useful to simplify the cloud classification, to facilitate the task and obtain precise results. The classification reduction is made by merging different cloud classes. To this end, a Student's *t*-test is adopted to compare the Clearness Index distributions, of each cloud type, with the respective of all the other Ct. Using the Matlab function *ttest2* [49] and setting the significance level, equal to 0.01, the previous 19 classes are aggregated into 4 new groups.

3. Machine learning models for short term forecasting

To archive the goal of this work and make the solar irradiance nowcasting 15 min ahead, Machine Learning techniques are used, exploiting satellite information and the meteorological data collected by the weather station at Solar Tech Lab.

3.1. Machine learning models

The Machine Learning techniques here adopted are the Single-Hidden Layer Feed Forward Neural Network plus Softmax function (SHLNN), the Double-Hidden Layer Feed Forward Neural Network plus Softmax function (DHLNN) with categorical and continuous data delivered in two different input layers, and the Random Forests (RF).

As described in Section 1, artificial neural networks are largely employed for irradiance and PV power forecasting. ANNs are capable of learning from a set of inputs data and expected outputs, in order to be able, at a later time, to make forecast on the basis of never seen input sets.

In this work, the neural networks are trained in a supervised way, where the algorithm analyzes the training data and produces an inferred function, which can be used for mapping new examples. This requires the learning algorithm to generalize from the training information in order to be able to predict conditions not seen during the training.

The SHLNN (Fig. 5) is a classical neural network, which presents the *Scaled Conjugate Gradient* as training algorithm, *Cross-entropy* as performance function, early stop and cross validation algorithms, and the hidden layer size is optimized to get the best performances.

At the input layer (green) all the incoming data are provided. After passing through the hidden layer (purple) the information converges in the SoftMax function. At the output layer (red) the vector of probability distributions of the potential outcomes is returned, and the class with the higher value corresponds to the network forecast.

The DHLNN network (Fig. 6) mainly differs from the previously described SHLNN for the presence of a second hidden layer and the location where inputs are provided to the network.

Considering the available data described below, two types of information can be passed to the neural network, i.e. continuous and categorical data. If both data types are provided together at once in the input layer, the network would encounter difficulties in learning their crucial differences even with a very large dataset available. One way to face this challenge is to divide the incoming data into two groups, one for each data typology, and supply them separately to the network. Going into detail, for this work a two hidden layer network is adopted, so it is decided to provide the categorical data in the first layer, while the continuous values are provided directly to the second hidden layer.
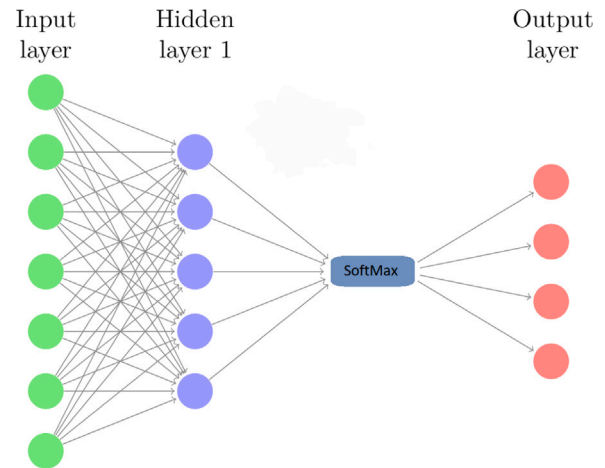

Fig. 5. Example of Feed Forward Single-Hidden Layer Neural Network implementing the SoftMax function for classification.
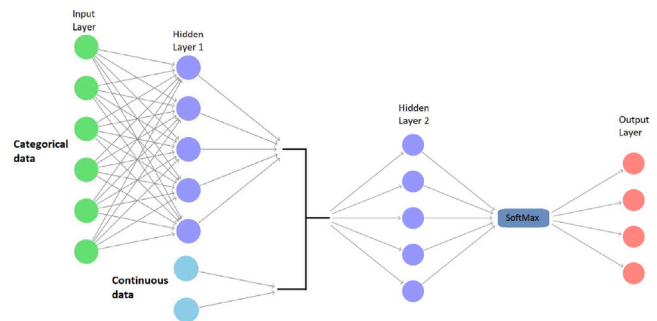

Fig. 6. Example of Feed Forward Double-Hidden Layer Neural Network topology.

As depicted in this Fig. 6, the categorical data are delivered in the first input layer (green), and analyzed by the first hidden layer (HL). The outgoing information from the first HL and the continuous data (light blue) are merged and provided to the second hidden layer. The *SoftMax* function and the output layer, are identical to the ones previously explained for the single hidden layer topology.

The last Machine Learning technique here adopted and presented is the Random Forests, which consists of an ensemble of decision trees. A full description of the algorithm can be found in [29] . In order to evaluate the prediction accuracy of the trees ensemble, the so called Out of Bag (OOB) score is here used. The available data is randomly sampled-with-replacement generating small subsets of the original data. These subsets, known as bootstrap samples, are shown in Figure 7. Each of these bootstrap samples is then fed as training to a single decision tree (DT) composing the random forest ensemble. This concept is known as Bagging or Bootstrap Aggregation.

OOB score can then be calculated as follows. For every DT, the available samples not used in the Bootstrap Samples are used in the OOB set. For example, in Figure 7 , 7 samples are available (A, B, C, D, E, F and G). The bootstrap samples used to train the first DT, DT1, are A, B, D and F (with replacement). Hence, the remaining samples (C, F and G) can be used in the OOB set to calculate the score.

The main difference between calculating the OOB score and a score on a validation set is that in the latter, a part of the original available dataset aside for validation purposes before training the models. Consequently, the OOB score is calculated using only a subset of DTs composing the forest not containing the OOB sample in their bootstrap training dataset. On the other hand, the validation score is calculated using all the DTs of the ensemble. This leads to a reduction in the overall ensemble beneficial effect in bagging. Thus, in general,
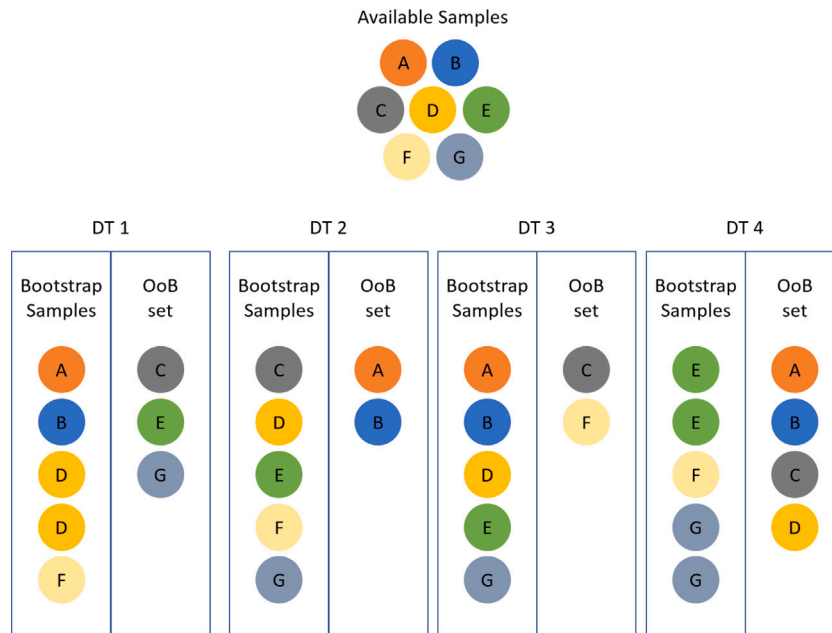
Fig. 7. Bootstrap aggregating process and Out of Bag sampling.

validation on a full ensemble of DTs is preferable than a subset of DT for estimating the score. However, if the dataset is composed by a small amount of data, setting aside a portion of it for validation purposes is not affordable. Consequently, in cases where the available dataset is limited the OOB score provides a good trade-off.

3.2. Sizing and performance evaluation algorithms

Concerning the neural networks, its sizing is performed to identify the optimal configuration of the hidden layers.

To this end, two different performance calculation procedures called "In-Bag Algorithm" (IBA), and "Out-of-Bag" (OOB) algorithm are designed. The IBA (Fig. 8(b)) changes the number of neutrons in the hidden layer from 1 to a maximum value. For each network topology configuration, the dataset available is first randomly divided into 70% training, 15% validation and the remaining 15% test. Then the average performance over ten independent trainings for each hidden layer configuration is evaluated. The OOB algorithm (Fig. 8(a)) changes the number of neurons in the hidden layer from 1 to a maximum value, as before. For each hidden layer configuration, one at time all the samples are separated from the whole training dataset. For each the Out-of-Bag samples, the remaining dataset is randomly divided using the 70% for training and the residual 30% for validation. The separated OOB sample is used to test the network and evaluate its performance, by providing it as input to the newly trained network, and comparing the neural network response with the corresponding target. To obtain reliable results, ten independent net trainings are executed for each OOB sample, and the average error is computed.

Once the optimal setups with both IBA and OOB algorithms are archived, the performances of the networks are evaluated through another "Out-of-Bag performance" (OOBp) algorithm. This new algorithm is identical to the OOB one explained above, but with the difference that the number of neurons in the hidden layer is no longer changed, but set to the optimum value previously identified. Thanks to this protocol network responses are independently obtained for all the single samples of the input dataset, without the network ever seeing the test sample, thus allowing to obtain robust results.

Table 1
Input dataset.

Set 1	Set 2	Set 3	Set 4	Set 5
α (t)	α (t)	α (t)	α (t)	α (t)
γ (t)	γ (t)	γ (t)	γ (t)	γ (t)
W_s (t)	W_s (t)	W_s (t)	W_s (t)	W_s (t)
W_d (t)	W_d (t)	W_d (t)	W_d (t)	W_d (t)
Rain (t)	Rain (t)	Rain (t)	Rain (t)	Rain (t)
K_T (t)	K_T (t)	K_T (t)	K_T (t)	K_T (t)
Circ.30 km (t)	Area $11 \times 6p$ (t)	Area $13 \times 7p$ (t)	Butterfly (t)	Full image (t)

4. Case study

This Section is focused on the construction of input and target datasets used to train the Machine Learning Models.

The available information for this work are the satellite images of ten representative days of 2019, and the meteorological data sampled by a weather station placed on the roof of the Energy department building of the Politecnico di Milano. More precisely the facility just mentioned collects data of Global Horizontal Irradiance, wind speed and direction, and rain intensity. In addition, also the solar angles (α, γ), calculated as above, and the Clearness Index computed with Eq. (1) are used.

Similarly to the approach followed for the cloud model, the asynchronism between the satellite information and the other data is overcome by averaging the values between 7 min before and 8 min after the respective satellite image time.

After removing all the measurements affected by errors or not suitable, the remaining data are combined in different ways to create various input datasets.

4.1. Input and target dataset

In order to identify the most suitable way to provide the information to the Machine Learning algorithms, five different input datasets are assembled (Table 1). While these datasets have in common some data, including α, γ, wind speed (W_s), wind direction (W_d), rain intensity and Clearness Index (K_T), they however differ areal extension of cloud type characterization, derived from satellite.
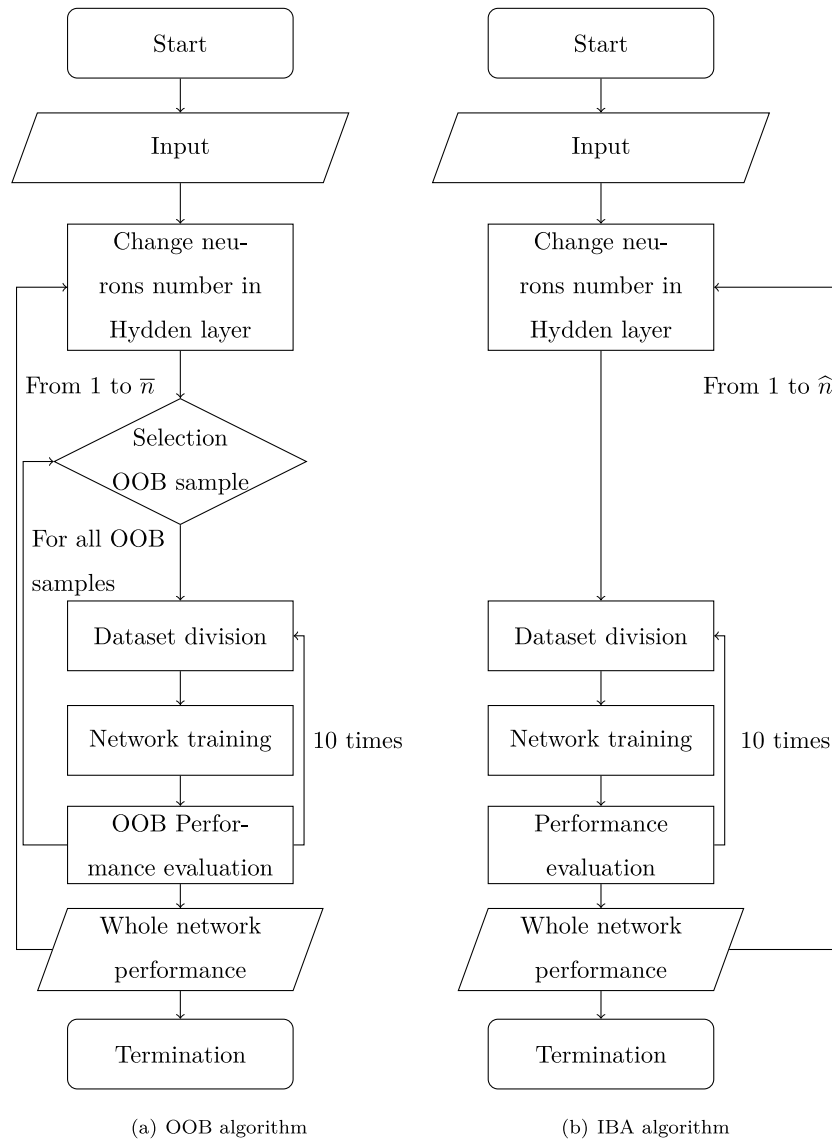
(a) OOB algorithm   (b) IBA algorithm

Fig. 8. IBA and OOB Algorithms flow chart.

The five tested configurations have the following characteristics: the first includes the satellite pixels contained in the circumference with radius equal to 30 km and centered at the Solar Tech Lab (Circ. 30 km); the second (Area 11 × 6p) includes a region south to the STL with an extension of 11 pixels east–west and 6 north–south; the third includes a region south to the STL with an extension of 13 pixels east–west and 7 north–south (Area 13 × 7p) and reported in Fig. 9(a); the fourth includes the 710 pixels intercepted by the solar diagram centered on the STL (Butterfly) and reported in Fig. 9(b); the last is the whole satellite picture 18 × 51 pixels (Full image).

In order to find the best way to deliver categorical data, the pixel cloud type information is provided in three different ways: in the first one the original classes are provided as integer input (Conf. 1); in the second one, a reduced classification based on the Student's t-test as above described is given (Conf. 2); finally, the third one provides the input in a One-Hot Encode format (Conf. 3). In Conf. 3 the One-Hot Encoding is introduced to provide the satellite data in a more suitable way for the forecasting algorithms. One Encode is used in Machine Learning as a method to quantify categorical data. Briefly, this method produces a vector with length equal to the number of categories in the dataset. If a data point belongs to the ith category, the value 0 is assigned to all the components of this vector except for the ith

Table 2
Proposed classes aggregation.

Original classes Conf. 1	Aggregated classes Conf. 2	Hot encode Conf. 3
1	1	[1, 0, 0, 0]
15, 19	2	[0, 1, 0, 0]
6, 8, 10, 16, 17, 18	3	[0, 0, 1, 0]
12, 14	4	[0, 0, 0, 1]

component, which is assigned a value of 1. For clarity, some examples are listed in Table 2 [50,51].

The dataset thus created is supplied to the neural networks in such a way as to deliver each element of each One Hot encode vector an input neuron. With reference to DHLNN (Fig. 6), the first input layer, the one that receives in input only the categorical data, is constituted by a number of input neurons equal to the number of pixels contained in the corresponding satellite image fraction multiplied by the size of the One Hot Encode vectors, i.e. 4.

The target value for the ML models is the Clearness Index K_T at $t+15$ min, where t represents the time of the correspondent inputs. The target values are divided in four classes, selected to be representative of
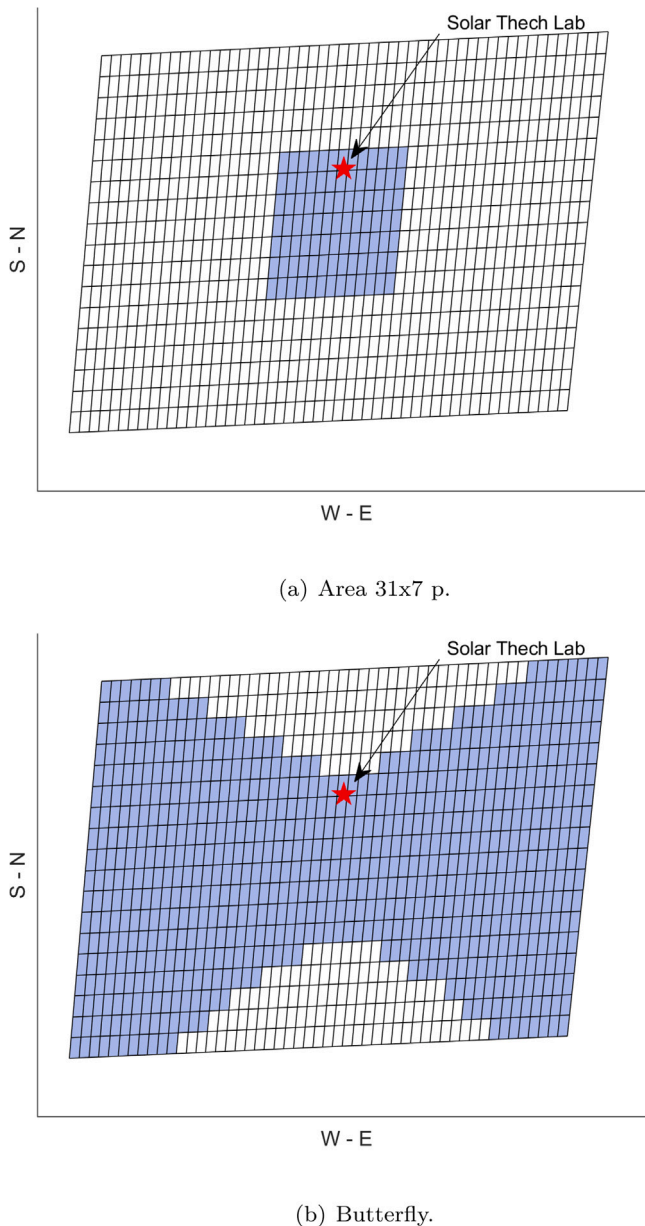
(a) Area 31x7 p.

(b) Butterfly.

Fig. 9. Satellite image fractions. The pixels highlighted in blue are the ones used to feed the models while the red star represents the location of the Solar Tech Lab. (a) Image fraction composed by 13×7 pixels respectively in direction W–E x N–S. (b) Image fraction composed by the 710 pixels intercepted by the solar diagram centered on the Solar Tech Lab.

Table 3
Output dataset subdivision..

Class	Interval	# of samples
C_1	$0 \leq K_T < 0.2$	43
C_2	$0.2 \leq K_T < 0.45$	44
C_3	$0.45 \leq K_T < 0.75$	98
C_4	$K_T \geq 0.75$	211

different sky conditions and, thus, of different operating conditions of PV power plants (Table 3). Worth noticing is that the boundaries among classes are statically and sharply defined. For this reason, values close to the limit between two classes could be critical in the classification phase. In the same table the number of available samples per class is provided.

5. Results

After assembling the input and target datasets, it is possible to train the different Machine Learning models. The following paragraphs will show for each ML model trained with each of the input dataset, the optimization procedure and the performance evaluation.

To better clarify the procedure adopted, a summary of the main steps followed for each Machine Learning techniques is illustrated in the following chart (Fig. 10).

5.1. Single-layer feed forward neural network

The optimization procedure is carried out with both the IBA and OOB algorithms described above. The number of hidden layers is varied between 1 and 300 for the IBA and between 1 to 50 for the OOB. These values are selected as a trade off between computational burden and accuracy of the final result. Once the optimal hidden layer is identified, the performance evaluation is made with the OOBp algorithm.

In general, for both the optimization algorithms, the results show that providing the satellite data in the Conf. 2 and Conf. 3 allows to get a performance increase between the 3% and 10% respect to Conf. 1, with the same input set. This certifies how the classification reduction implies the elimination of information not useful for the neural network in order to perform its task.

Among all the input data configurations investigated, the best is the one distinguished by the "Butterfly" portion of the satellite image in Conf. 3, which gets 80.3% of Total success rate, and it is optimized with IBA algorithm. The confusion matrix in Fig. 11 shows good results: most of the values fall on the diagonal, while the few errors made by the network lie almost entirely around the diagonal. The mistaken exchange of two non-adjacent target classes is limited to very few units (3.1%), while it never happens that the network confuses the two classes at the antipodes, i.e. C_1 and C_4.

Fig. 12 shows another graph useful to analyze the performance of the network. It reports three curves: the sorted performance from worst to best, the average one, and the cumulative performance curve.

In the performance curve, the maximum value is lower than 0.5, and it is reached only by two samples, after which a rapid decrease is noticed. Exceeding the 100th sample, the performance values are below average (0.08). This underlines that almost all of the error is concentrated in a small minority of data. The cumulative error line, with an increasing slope that reaches the 95% of error around the sample number 140, further confirms it. Indeed, after that the curve tends to flatten out and remains constant for all the remaining samples.

5.2. Double-layer feed forward neural network

The main differences from the single layer network are the presence of a second hidden layer and the location where inputs are provided. The division of the categorical and continuous input data is more effective if the categorical information is provided in one encode format. Indeed, this procedure makes it clearer to the algorithm that the data provided are categorical. Therefore, only Conf. 3 is adopted for this network topology.

Similarly to the single layer NN approach, both the OOB and IBA algorithms for the network optimization and the OOBp for the performance evaluation are used. In this case the number of hidden layers is varied between 1 and 50 for the IBA, and between 1 to 20 for the OOB, because of the higher computation burden of this topology.

The results of the two optimization algorithms are very similar, with slightly higher values for the networks optimized with the OOB algorithm.

The best performance is reached by the input set characterized by the "Butterfly" portion of satellite data optimized with the OOB algorithm, which gets 80.8% of Total success rate. To better analyze
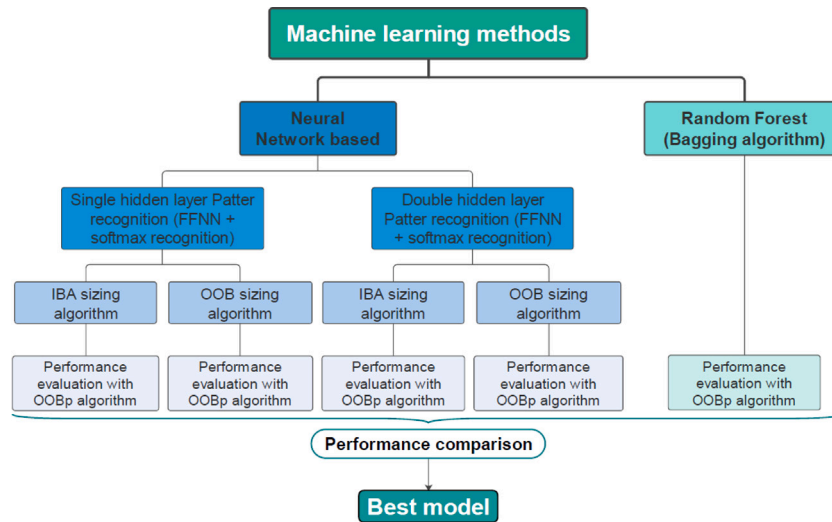
Fig. 10. Outline of the main steps followed for training and performance evaluation of the three Machine Learning methods adopted.

Fig. 11. Confusion Matrix of Set 4 Conf.3 NN optimized with IBA algorithm.

these outcomes, in the following is reported the confusion matrix (Fig. 13) of the most performing network.

The confusion matrix shows good results: most of the values fall on the diagonal, while the few errors made by the network (19.2%) lie almost entirely around the diagonal.

The mistaken exchange of two non-adjacent target classes is limited to very few units (2.4%), while it never happens that the network confuses the two classes at the antipodes, i.e. C_1 and C_4.

Another way to investigate the network performance is reported in Fig. 14, where the sorted performance curve, the average performance and the cumulative one are shown.

The blue bars have the highest value close to 1.6 and a following sharp decrease, which leads to have its values below the average (0.15) after the 90th sample. This means that most of the error is concentrated in a portion of the dataset, and this is also confirmed by the cumulative curve, which has a sharp increase for the first samples, reaching the 95% of the error around the 170th sample.

5.3. Random forests

Due to the simplicity of the Random Forests, the only parameter set is the number of grown trees. For the first attempt a value is arbitrary selected, and after the first run the value is adjusted to allow each model to reach the minimum error. The optimal number of trees is identified in the configuration that provides the lower out of bag error. To obtain reliable results, for each Random Forest ten independent runs are made averaging the errors and the performance thus obtained.

All the input datasets configurations previously described are adopted to investigate which one provides better information. All the input configurations provide results above the 81% of total success rate, therefore the worst result recorded here is better than the best performance recorded by neural networks (80.8%). The gap between Conf. 1 and Conf. 2–3, observed in the single layer neural networks, is no longer present thanks to the better ability of the Random Forests to filter the useless information and the noise present in the data analyzed. The input dataset with the best total success rate is the one characterized by the "Area 13 × 7p" in Conf. 1. with 84.2%.

In the following the out-of-bag error for each grown tree chart (Fig. 15), and the confusion matrix (Fig. 16) of this input dataset are reported.

The blue line depicted in Fig. 15 is representative of the error committed by the RF model as a function of the number of the DT composing the ensemble. It presents a sharp decreasing trend for the first 20 trees that tend to decline asymptotically reaching the minimum at 375 trees with an OOB error equal to 0.16 (Red spot). As stated in [29], this occurs because the marginal benefits of introducing a new DT in the ensemble is less impacting when the number of DT is already significant. This leads to the RF converging asymptotically to an error as the number of trees in the forest becomes large. The rate of convergence greatly depends on the strength of the individual trees in the forest and the correlation between them. In Figure 15 it is possible to notice that the error does not monotonically decrease. Due to the high complexity of the meteorological phenomenon involved and the limited amount of input data available, poorly trained DT might be in the ensemble, leading to a small increase of the error committed. As noticeable, though, their impact is mitigated increasing the number of trees. On the other hand, increasing the number of trees lead to high computational burden of the RF. For this reason, a trade-off between the required accuracy and the computational time is required which led the author to 375 trees.

Looking at the confusion matrix reported in Fig. 16, it appears evident the goodness of the results. In addition to the high percentage of
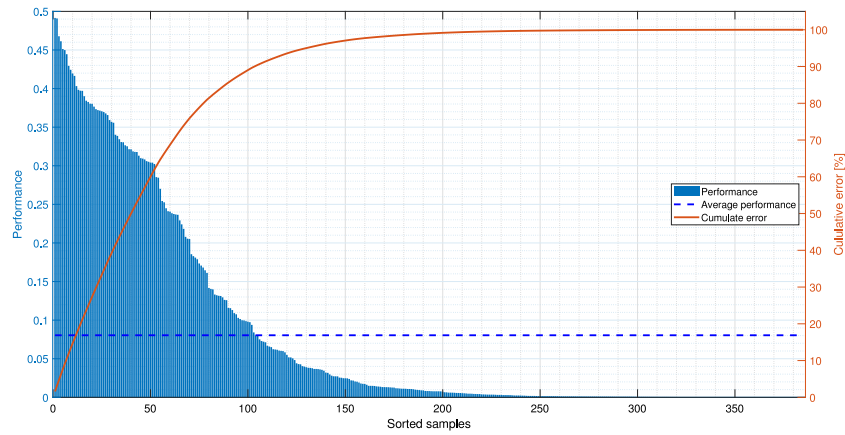
Fig. 12. Performance and cumulative error for Set 4 - Conf.3, IBA configuration. The blue bars represent the sorted performance of each sample of the dataset, the dotted line is the average performance over the whole dataset, and the orange line is the cumulative error of the sorted performance.

Fig. 13. Confusion Matrix of Set 4 optimized with OOB algorithm.

Table 4
Machine Learning model comparison.

Input configurations	Accuracy		
	SHLNN	DHLNN	RF
Conf. 1	72.5%	–	84.2%
Conf. 2	79.7%	–	83.1%
Conf. 3	80.3%	80.8%	83.1%

reduced to 4 by means of a t-test clustering approach, and Conf. 3 in which the four clustered groups are provided to the Neural Network in one-hot-encode.

All the ML models and input configurations have been tested on the same dataset, and the accuracy results provided in the Table are obtained with an OOB testing approach that guarantees a great robustness.

The results provided in Table 4 shows two important aspects. First of all, the input clustering highly improves the classification accuracy for Neural Networks, while for the Random Forest it decreases of approximately 1% the performance. Secondly, the DHLNN outperforms the simpler SHLNN, with a slight increase of the training computational effort.

6. Conclusions

The main goal of this work is to forecast the correct clearness index class of a geographic target (here the Solar Tech Lab) 15 min ahead exploiting Machine Learning techniques. To the scope, the performances of SHLNN. DHLNN and RF are analyzed.

In order to achieve the goal of the work, a new cloud model is introduced. It shows excellent results in the identification of clouds that interfere with solar radiation. A new cloud type classification is also introduced to feed neural networks, leading to up to 10% improvement in the prediction performances.

The IBA and OOB algorithms designed for the neural network optimization provide similar results. The first one has the advantage to be simple and fast, but it suffers from noisy data, while the latter has excellent ability to filter any noise in the data, at the expense of a higher computational burden.

These considerations show how all the three Machine Learning Methods provide excellent results, compared also to the limited dataset available. However, Random Forests has a fair advantage from a performance point of view and a clear advantage from a computational point of view. Furthermore, it is highlighted that neural networks need a large portion of satellite data, provided in a restricted and therefore coarse classification, while Random Forests require a smaller portion of the satellite image, but with a more detailed classification.
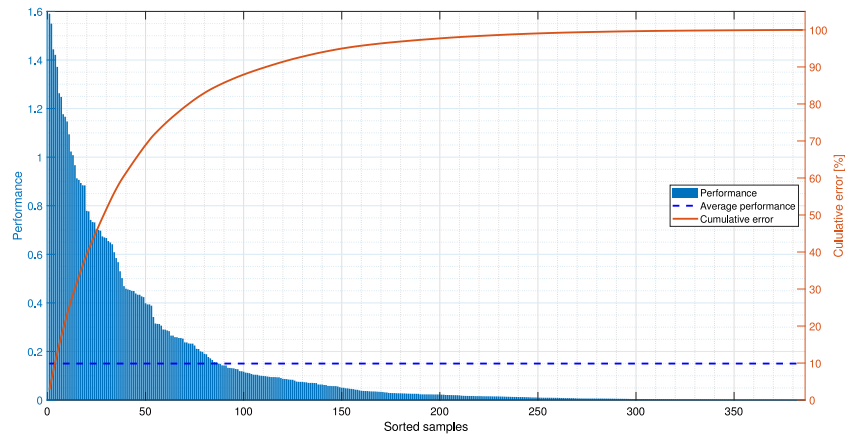
correctly classified samples, the errors committed are of limited magnitude. All samples not correctly classified are confused with an adjacent class, while there are no exchanges between two non-neighboring groups.

This highlights how Random Forests are able to get very good performances with few but detailed data respect to the NNs which need a bigger portion of the satellite image to get comparable results.

5.4. Comparison between models and discussion

In this paper three different Machine Learning models have been tested for performing the nowcasting exploiting satellite data and a new cloud model. All the results previously presented in this Section have been summarized in Table 4 for discussing the obtained results. The table shows the results all the three models (SHLNN — Single Hidden Layer Neural Network, DHLNN — Double Hidden Layer Neural Network, and RF — Random Forest) on the three different tested input dataset: Conf. 1 in which the original 19 classes are provided with a integer-value representation, Conf. 2 where the classes have been

Fig. 14. Performance and cumulative error for Set 4, OOB configuration. The blue bars represent the sorted performance of each sample of the dataset, the dotted line is the average performance over the whole dataset, and the orange line is the cumulative error of the sorted performance.
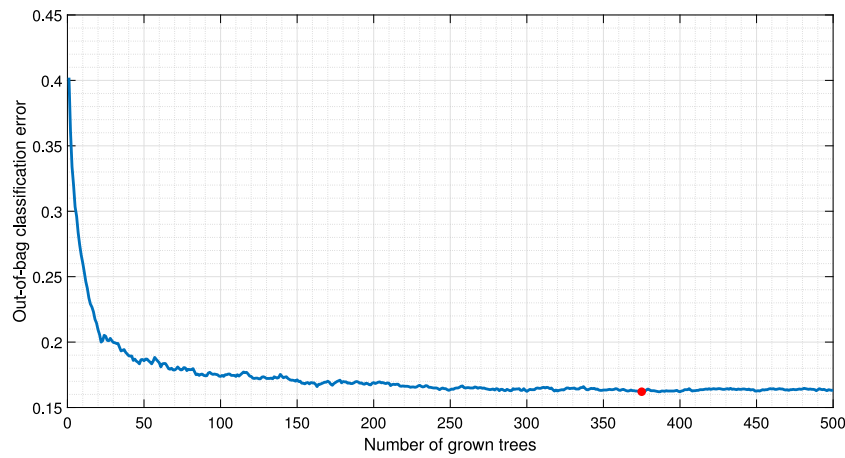

Fig. 15. Out-of-Bag error of Set 3 in Conf. 1.

Fig. 16. Confusion Matrix of Set 3 in Conf. 1.

Despite the excellent performance provided by all the three Machine Learning models, they still commit some misclassification error. The errors committed are common to all models even if in different quantities. The first and most important misclassification type is the confusion of two adjacent target classes due to the proximity of the K_T target value to the rigid border between them. The second is the occurrence of particular atmospheric conditions difficult to detect such as multiple layers of different clouds types or the presence of an uneven cloud cover composed of small clouds which continuously change shape and size. It is then clear that the majority of the errors are attributable to the presence of borderline cases or to a non-optimal subdivision of the target dataset, and therefore they are not attributable to poor network training.

In order to improve the present results in future works, some proposals are here presented.

The Cloud model could be improved by increasing the accuracy in the modeling of the properties of the clouds, such as the physical phase of the cloud (ice or water) and its optical thickness, because these are important factors in the attenuation of incident radiation.

For the Machine Learning Models, most of the errors are due to the rigid classification of the target dataset. A mitigation strategy could involve the adoption of fuzzy logic classification, or the introduction of confidence interval, which can reduce the effect rigid boundaries. For the borderline weather conditions mentioned above, the adoption of a larger training dataset could help the network to learn how to better classify these conditions.

In summary this work shows how the use of Machine Learning techniques, which exploit satellite data and weather information, provides

important and significant results in the prediction of solar radiation fifteen minutes ahead on a specific geographic target. In addition to the excellent results obtained, various improvements are proposed aiming at further increasing the network performance with future works.

Declaration of competing interest

The authors declare that they have no known competing financial interests or personal relationships that could have appeared to influence the work reported in this paper.

Acknowledgment

References

[1] Yin X, Li J, Kadry SN, Sanz-Prieto I. Artificial intelligence assisted intelligent planning framework for environmental restoration of terrestrial ecosystems. Environ Impact Assess Rev 2021;86(2020):106493. http://dx.doi.org/10.1016/j.eiar.2020.106493.

[2] Varzaneh SG, Raziabadi A, Hosseinzadeh M, Sanjari MJ. Optimal energy management for PV-integrated residential systems including energy storage system. IET Renew Power Gener 2021;15(1):17–29. http://dx.doi.org/10.1049/rpg2.12002.

[3] Pandit RK, Kolios A, Infield D. Data-driven weather forecasting models performance comparison for improving offshore wind turbine availability and maintenance. IET Renew Power Gener 2020;14(13):2386–94. http://dx.doi.org/10.1049/iet-rpg.2019.0941.

[4] Liu Y, Gao X, Yan J, Han S, Infield DG. Clustering methods of wind turbines and its application in short-term wind power forecasts. J Renew Sustain Energy 6 (5). http://dx.doi.org/10.1063/1.4898361.

[5] Ahmed R, Sreeram V, Mishra Y, Arif MD. A review and evaluation of the state-of-the-art in PV solar power forecasting: Techniques and optimization. Renew Sustain Energy Rev 2019;124. http://dx.doi.org/10.1016/j.rser.2020.109792.

[6] Yang D, Kleissl J, Gueymard CA, Pedro HT, Coimbra CF. History and trends in solar irradiance and PV power forecasting: A preliminary assessment and review using text mining. Sol Energy 2018;168:60–101. http://dx.doi.org/10.1016/j.solener.2017.11.023.

[7] Verbois H, Huva R, Rusydi A, Walsh W. Solar irradiance forecasting in the tropics using numerical weather prediction and statistical learning. Sol Energy 2018;162(2017):265–77. http://dx.doi.org/10.1016/j.solener.2018.01.007.

[8] Liang X. Emerging power quality challenges due to integration of renewable energy sources. IEEE Trans Ind Appl 2017;53(2):855–66. http://dx.doi.org/10.1109/TIA.2016.2626253.

[9] Bajaj M, Singh AK. Grid integrated renewable DG systems: A review of power quality challenges and state-of-the-art mitigation techniques. Int J Energy Res 2020;44(1):26–69. http://dx.doi.org/10.1002/er.4847.

[10] Moretti L, Polimeni S, Meraldi L, Raboni P, Leva S, Manzolini G. Assessing the impact of a two-layer predictive dispatch algorithm on design and operation of off-grid hybrid microgrids. Renew Energy 2019;143:1439–53. http://dx.doi.org/10.1016/j.renene.2019.05.060.

[11] Ogliari E, Niccolai A, Leva S, Zich RE. Computational intelligence techniques applied to the day ahead PV output power forecast: PHANN, SNO and mixed. Energies 2018;11(6):121693718. http://dx.doi.org/10.3390/en11061487.

[12] Chen SX, Gooi HB, Wang MQ. Sizing of energy storage for microgrids. IEEE Trans Smart Grid 2012;3(1):142–51. http://dx.doi.org/10.1109/TSG.2011.2160745.

[13] Lee S, Jin H, Vecchietti LF, Hong J, Har D. Short-term predictive power management of PV-powered nanogrids. IEEE Access 2020;8:147839–57. http://dx.doi.org/10.1109/access.2020.3015243.

[14] Khalili T, Jafari A, Abapour M, Mohammadi-Ivatloo B. Optimal battery technology selection and incentive-based demand response program utilization for reliability improvement of an insular microgrid. Energy 2019;169:92–104. http://dx.doi.org/10.1016/j.energy.2018.12.024.

[15] Mellit A, Pavan AM, Ogliari E, Leva S, Lughi V. Advanced methods for photovoltaic output power forecasting: A review, Applied Sciences (Switzerland) 10 (2). http://dx.doi.org/10.3390/app10020487.

[16] Chen X, Du Y, Lim E, Wen H, Jiang L. Sensor network based PV power nowcasting with spatio-temporal preselection for grid-friendly control. Appl Energy 2019;255(May):113760. http://dx.doi.org/10.1016/j.apenergy.2019.113760.

[17] Diagne M, David M, Lauret P, Boland J, Schmutz N. Review of solar irradiance forecasting methods and a proposition for small-scale insular grids. 2013, http://dx.doi.org/10.1016/j.rser.2013.06.042.

[18] Voyant C, Notton G, Kalogirou S, Nivet ML, Paoli C, Motte F, et al. Machine learning methods for solar radiation forecasting: A review. Renew Energy 2017;105:569–82. http://dx.doi.org/10.1016/j.renene.2016.12.095.

[19] Antonanzas J, Osorio N, Escobar R, Urraca R, Martinez-de Pison FJ, Antonanzas-Torres F. Review of photovoltaic power forecasting. 2016, http://dx.doi.org/10.1016/j.solener.2016.06.069.

[20] Schmidt T, Calais M, Roy E, Burton A, Heinemann D, Kilper T, et al. Short-term solar forecasting based on sky images to enable higher PV generation in remote electricity networks. Renew Energy Environ Sustain 2017;2:23. http://dx.doi.org/10.1051/rees/2017028.

[21] Bright JM, Killinger S, Lingfors D, Engerer NA. Improved satellite-derived PV power nowcasting using real-time power data from reference PV systems. Sol Energy 2018;168(2017):118–39. http://dx.doi.org/10.1016/j.solener.2017.10.091.

[22] Catalina A, Alaiz CM, Dorronsoro JR. Combining numerical weather predictions and satellite data for PV energy nowcasting. IEEE Trans Sustain Energy 2020;11(3):1930–7. http://dx.doi.org/10.1109/TSTE.2019.2946621.

[23] Barbieri F, Rajakaruna S, Ghosh A. Very short-term photovoltaic power forecasting with cloud modeling: A review. Renew Sustain Energy Rev 2017;75(November 2016):242–63. http://dx.doi.org/10.1016/j.rser.2016.10.068.

[24] Dolara A, Leva S, Manzolini G. Comparison of different physical models for PV power output prediction. Sol Energy 2015;119:83–99. http://dx.doi.org/10.1016/j.solener.2015.06.017.

[25] Manogaran G, Lopez D. Spatial cumulative sum algorithm with big data analytics for climate change detection. Comput Electr Eng 2018;65:207–21. http://dx.doi.org/10.1016/j.compeleceng.2017.04.006.

[26] Mellit A, Kalogirou SA. Artificial intelligence techniques for photovoltaic applications: A review. Prog Energy Combust Sci 2008;34(5):574–632. http://dx.doi.org/10.1016/j.pecs.2008.01.001.

[27] Mellit A, Pavan AM. A 24-h forecast of solar irradiance using artificial neural network: Application for performance prediction of a grid-connected PV plant at Trieste, Italy. Sol Energy 2010;84(5):807–21. http://dx.doi.org/10.1016/j.solener.2010.02.006.

[28] Siddiqui TA, Bharadwaj S, Kalyanaraman S. A deep learning approach to solar-irradiance forecasting in sky-videos. In: Proceedings - 2019 IEEE winter conference on applications of computer vision, WACV 2019. 2019, p. 2166–74. http://dx.doi.org/10.1109/WACV.2019.00234, arXiv:1901.04881.

[29] Breiman L. Random forests. Mach Learn 2001;45(1):5–32. http://dx.doi.org/10.1023/A:1010933404324.

[30] Fawagreh K, Gaber MM, Elyan E. Random forests: From early developments to recent advancements. Syst Sci Control Eng 2014;2(1):602–9. http://dx.doi.org/10.1080/21642583.2014.956265.

[31] Tato JH, Brito MC. Using smart persistence and random forests to predict photovoltaic energy production. Energies 2019;12(1):1–12. http://dx.doi.org/10.3390/en12010100.

[32] Meng M, Song C. Daily photovoltaic power generation forecasting model based on random forest algorithm for north china in winter. Sustainability (Switzerland) 12 (6). http://dx.doi.org/10.3390/su12062247.

[33] Acevedo YVN, Marin CEM, Garcia PAG, Crespo RG. A proposal to a decision support system with learning analytics. In: IEEE global engineering education conference, EDUCON 2018-April. 2018, p. 161–8. http://dx.doi.org/10.1109/EDUCON.2018.8363223.

[34] Akhter MN, Mekhilef S, Mokhlis H, Shah NM. Review on forecasting of photovoltaic power generation based on machine learning and metaheuristic techniques. IET Renew Power Gener 2019;13(7):1009–23. http://dx.doi.org/10.1049/iet-rpg.2018.5649.

[35] Dolara A, Grimaccia F, Leva S, Mussetta M, Ogliari E. A physical hybrid artificial neural network for short term forecasting of PV plant power output. Energies 2015;8(2):1138–53. http://dx.doi.org/10.3390/en8021138.

[36] Niccolai A, Nespoli A. Sun position identification in sky images for now-casting application. Forecasting 2020;2(4):488–504. http://dx.doi.org/10.3390/forecast2040026.

[37] Nikitidou E, Kazantzidis A, Tzoumanikas P, Salamalikis V, Bais AF. Retrieval of surface solar irradiance, based on satellite-derived cloud information, in Greece. Energy 2015;90:776–83. http://dx.doi.org/10.1016/j.energy.2015.07.103.

[38] Quesada-Ruiz S, Chu Y, Tovar-Pescador J, Pedro HT, Coimbra CF. Cloud-tracking methodology for intra-hour DNI forecasting. Sol Energy 2014;102:267–75. http://dx.doi.org/10.1016/j.solener.2014.01.030.

[39] Bright JM, Killinger S, Lingfors D, Engerer NA. Improved satellite-derived PV power nowcasting using real-time power data from reference PV systems. Sol Energy 2018;168(August 2017):118–39. http://dx.doi.org/10.1016/j.solener.2017.10.091.

[40] Khosravi A, Koury RN, Machado L, Pabon JJ. Prediction of hourly solar radiation in Abu Musa Island using machine learning algorithms. J Cleaner Prod 2018;176:63–75. http://dx.doi.org/10.1016/j.jclepro.2017.12.065.

[41] Kumar DS, Yagli GM, Kashyap M, Srinivasan D. Solar irradiance resource and forecasting: A comprehensive review. IET Renew Power Gener 2020;14(10):1641–56. http://dx.doi.org/10.1049/iet-rpg.2019.1227.

[42] Li J, Ward JK, Tong J, Collins L, Platt G. Machine learning for solar irradiance forecasting of photovoltaic system. Renew Energy 2016;90:542–53. http://dx.doi.org/10.1016/j.renene.2015.12.069.

[43] Jang HS, Bae KY, Park HS, Sung DK. Solar power prediction based on satellite images and support vector machine. IEEE Trans Sustain Energy 2016;7(3):1255–63. http://dx.doi.org/10.1109/TSTE.2016.2535466.

[44] Engerer NA, Bright JM, Killinger S. Himawari-8 Enabled Real-Time Distributed Pv Simulations for Distribution Networks (December) (2018) 1405–1410. http://dx.doi.org/10.1109/pvsc.2017.8521518.

[45] Schmetz J, Pili P, Tjemkes S, Just D, Kerkmann J, Rota S, et al. Supplement to an introduction to meteosat second generation (MSG). Bull Am Meteorol Soc 2002;83(7):991. http://dx.doi.org/10.1175/bams-83-7-schmetz-1.

[46] Marcos C, Rodríguez A, Calbet X, Rípodas P. Algorithm theoretical basis document for the precipitation product processors of the NWC / GEO, vol. 154. (October):Nwcsaf, Eumetsat; 2016, p. 63, www.nwcsaf.org.

[47] Stein JS, Holmgren WF, Forbess J, Hansen CW. PVLIB: Open source photovoltaic performance modeling functions for Matlab and Python. In: 2016 IEEE 43rd photovoltaic specialists conference (PVSC). 2016, p. 3425–30. http://dx.doi.org/10.1109/PVSC.2016.7750303.

[48] Yang D. Choice of clear-sky model in solar forecasting. J Renew Sustain Energy 2020;12(2):026101. http://dx.doi.org/10.1063/5.0003495, http://aip.scitation.org/doi/10.1063/5.0003495.

[49] Wang X-p, Shi M-x. Matlab for forecasting of electric power load based on BP neural network. In: Chen R, editor. Intelligent computing and information science. Berlin, Heidelberg: Springer Berlin Heidelberg; 2011, p. 636–42. http://dx.doi.org/10.1007/978-3-642-18129-0_96.

[50] Karthiga R, Usha G, Raju N, Narasimhan K. Transfer learning based breast cancer classification using one-hot encoding technique. In: Proceedings - International conference on artificial intelligence and smart systems, ICAIS 2021. 2021, p. 115–20. http://dx.doi.org/10.1109/ICAIS50930.2021.9395930.

[51] Li J, Si Y, Xu T, Jiang S. Deep convolutional neural network based ECG classification system using information fusion and one-hot encoding techniques. Math Probl Eng 2018. http://dx.doi.org/10.1155/2018/7354081.